Journal of the Ceramic Society of Japan 122 [10] 863-869 2014 Paper

Improvement in matrix microstructure of SiC/SiC composites by incorporation of pore-forming powder

Masaki KOTANI,† Aline ZIMMER,* Satoru MATSUZAKI, Kazuaki NISHIYABU*** and Shigeo TANAKA****

Japan Aerospace Exploration Agency, 6–13–1 Osawa, Mitaka, Tokyo 181–0015, Japan
***University of Stuttgart, Pfaffenwaldring 31, 70569 Stuttgart, Germany**
****Taisei Kogyo Co. Ltd., 26–1 Ikeda-kita, Neyagawa, Osaka 572–0073, Japan**
*****Kinki University, 3–4–1 Kowakae, Higashiosaka, Osaka 577–8502, Japan**

In order to improve the matrix microstructure of SiC-fiber-reinforced SiC matrix (SiC/SiC) composite, the authors examined a combination process involving the polymer impregnation and pyrolysis (PIP) process and a pore-producing treatment that incorporates a pore-forming agent into the matrix precursor. Unidirectional SiC/SiC composites were fabricated under such conditions of selected slurry preparation that a good porous monolith could be obtained. A porous matrix base was formed relatively uniformly in both the intra- and the inter-bundle region in the first PIP processing, and subsequently densified efficiently by repetitive process cycles of PIP. By comparing the resulting composites with those fabricated via the conventional PIP process, it was verified that this newly attempted fabrication process is advantageous in lowering the porosity, particularly by reducing the size of the intra-bundle pores, and leads to an improvement in some representative mechanical properties.

©2014 The Ceramic Society of Japan. All rights reserved.

Key-words : Polymer impregnation and pyrolysis, Matrix microstructure, Porous structure, Densification, Mechanical properties

[Received March 28, 2014; Accepted July 13, 2014]

1. Introduction

SiC/SiC composites are important candidates for high-temperature structural materials used in engine components such as the combustor liner, turbine brisk and thruster nozzle, as well as the air-frame parts of hypersonic aircraft and reusable space transportation systems subjected to a middle to high heat load.[1)–6)]

Among the various fabrication processes of SiC/SiC composites, the polymer impregnation and pyrolysis (PIP) process is advantageous especially in terms of its applicability to the fabrication of large-scale and complex-shaped components because it has many similarities to both the fabrication techniques and facilities of carbon fiber reinforced plastic (CFRP). It is also attractive because it enables a wide-range control of the microstructure.[7)–10)] However, when a precursor polymer impregnated in a fiber preform is pyrolyzed, gas evolution and volume shrinkage inevitably occur and consequently many pores and cracks are generated in the matrix. Even when subjected to subsequent processing, the matrix containing those defects can be densified only to a limited degree.[11),12)] Matrix defects should be reduced to enhance matrix-dependent properties such as interlaminar strengths and airtightness. The densification and reduction of matrix defects also contribute to the enhancement of tensile strength along the fiber direction by increasing the fiber-to-matrix load transfer capability, according to Curtin's theory.[13)] Therefore, a structure that is initially formed in a fiber preform should be highly uniform and continuous. This challenge on matrix formation has not yet been sufficiently dealt with and needs to be addressed to enable wide industrial application.

With the above motivation in mind, we designed a new PIP process to form a better matrix using the following concepts: i) a good matrix base should be formed at first; ii) it should be structurally continuous in three dimensions; iii) spaces generated by polymer pyrolysis should be finely and uniformly dispersed into round-shaped pores rather than sharp cracks. The new PIP process developed by us could form a uniform and fine porous structure in the first PIP processing, as is schematically illustrated in **Fig. 1**. In order to create a porous structure in a polymer-pyrolyzed product, pore-forming powder was mixed with polymer precursor and was removed by heating after the polymer hardening. This method has been widely used in metal injection molding to produce porous metal materials and is sometimes called the powder space holding (PSH) method.[14),15)] Hence, the currently proposed PIP process incorporating the PSH method during its first processing stage is termed "PSH-PIP".

Initially, the mixing conditions of the pore-forming powder into the polymer precursor were investigated by preparing monoliths. Using a systematic research method, the optimum condition for slurry preparation was found.[16)] While pyrolyzed products are normally formed with a lot of cut-through crack initiation and consequently break into pieces even when mixed with some inert particles, we were able to produce a stable polymer-derived porous body using our process.

In this study, we examine the applicability of the PSH-PIP process to composite fabrication and its effects on microstructure and mechanical properties. Unidirectional composites were fabricated using the PSH-PIP process and, for comparison, the conventional PIP (abbreviated hereafter as conv. PIP) process under the best conditions of each process. Composite fabrication using the PSH-PIP process consists of the following two stages: 1) formation of a porous matrix base by mixing pore-forming powder into a precursor polymer during the initial PIP processing and 2) densification of the matrix base by repeating normal PIP processing. The composites were evaluated and compared by performing microstructural analyses, densitometry, and some mechanical tests.

† Corresponding author: M. Kotani; E-mail: kotani.masaki@jaxa.jp

©2014 The Ceramic Society of Japan
DOI http://dx.doi.org/10.2109/jcersj2.122.863

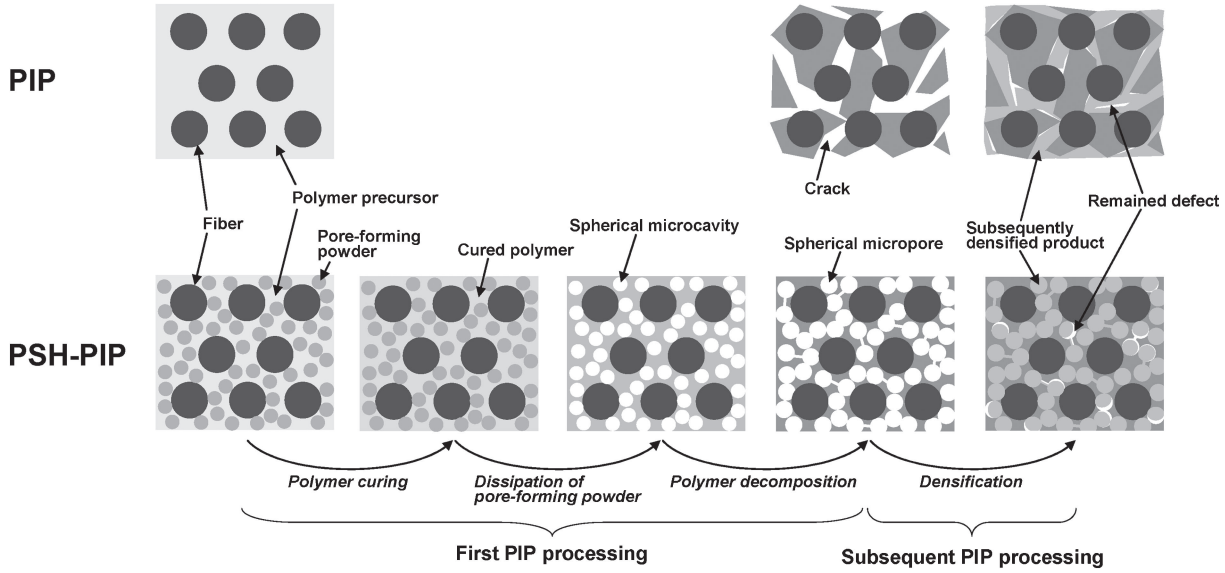

Fig. 1. Schematic illustration of SiC/SiC composite microstructures obtained by the PSH-PIP process.

Table 1. Properties of the composites obtained by various measurements

Measurement	Property	Conv. PIP (300 nm)[a]	PSH-PIP (300 nm)	PSH-PIP (100 nm)
Dimensions and weight	Fiber volume fraction/%	24	22	22
Densitometry	Bulk density/g·cm^{-3}	1.95	1.96	2.06
	Open porosity/%	18.5	13.2	11.0
Internal friction	Internal friction/–	1.1E-03	7.7E-04	8.0E-04
Transverse tension	Ultimate strength/MPa	1.46 (1.26)[b]	3.64 (2.26)	3.19 (1.95)
Longitudinal tension	Ultimate strength/MPa	305 (64)	348 (44)	347 (33)
	Strain at fracture/%	0.27 (0.087)	0.39 (0.154)	0.32 (0.041)
	Elastic modulus[c]/GPa	113 (1.1)	120 (1.4)	116 (1.9)
Longitudinal compression	Ultimate strength/MPa	501 (78)	495 (98)	361 (85)
	Strain at fracture/%	0.72 (0.105)	0.72 (0.104)	0.55 (0.11)
	Elastic modulus[d]/GPa	77 (5.5)	71 (3.4)	68 (6.9)
Longitudinal SENB	Fracture toughness/MPa·m$^{1/2}$	6.17 (0.91)	9.56 (1.89)	9.91 (0.63)

a Carbon layer thickness.
b The values in parentheses represent standard deviations.
c Tangent moduli in the range of 0–100 MPa.
d Tangent moduli in arbitrary linear sections of range 40 MPa within 100–300 MPa.

2. Experimental procedures

Materials used for the composite fabrication were as follows. A bundle of Tyranno fiber® ZMI-grade supplied by Ube Industry, Ltd. (Japan) was used for the reinforcement. It consisted of 800 filaments with an average diameter of 11 μm. For the matrix polymer precursor, allylhydridopolycarbosilane (AHPCS) SMP-10 from Starfire® Systems Inc. (US) was used because it is liquid at room temperature and has high ceramic yield and SiC purity. For the pore-forming powder, polymethylmethacrylate (PMMA) particles of an average diameter of 10 μm, Chemisnow® MX-100, from Soken Chemical & Engineering Co., Ltd. (Japan) was used. For the filler material used only in the conv. PIP process, a powder of SiC particles with an average diameter of 0.27 μm, Beta random ultra-fine grade, from IBIDEN Co., Ltd. (Japan) was applied.

Composites were fabricated in the following steps: (1) the fiber bundles were wound on carbon fixtures uniformly at the pitch of about 0.83 mm to fabricate unidirectional fibrous sheets; (2) interface layers were formed on the fiber surface of the sheets using chemical vapor infiltration (CVI); (3) polymeric slurry was prepared by mixing the materials; (4) the fibrous sheets were immersed in the slurry to form prepreg sheets; (5) eight prepreg sheets were cut, stacked and then bagged; (6) the stacked prepreg sheets were cured at 130°C under vacuum for more than 10 h to form a green body; (7) the green body was pyrolyzed at temperatures of up to 1000°C under argon atmosphere to form a porous-matrix composite; and (8) the porous-matrix composite was densified by repeating the impregnation and pyrolysis with only the liquid polymer 6 times. Eventually, unidirectional composite plates approximately 160 mm square and approximately 4 mm thick were obtained. Fiber volume fractions of all the composites, obtained using the weights and densities of the fiber and the external dimensions of the composites, were 22–24% (see **Table 1**). Representative photographs of the composite fabrication are shown in **Fig. 2**.

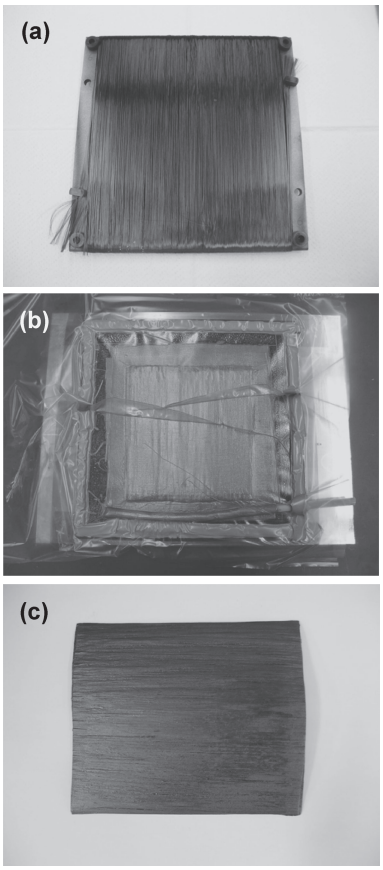

Fig. 2. Representative photographs of the PSH-PIP process: (a) Fibrous sheets wound on a carbon fixture, (b) Bagged prepreg sheets in vacuum, (c) Unidirectional composite after the sixth densification process.

Interface layers consisting of inner carbon layers and outer SiC layers were used. Two kinds of fiber preform were prepared for the PSH-PIP process, one with a carbon layer thickness of 100 nm and another with a thickness of 300 nm while the fiber preform prepared for the conv. PIP process used a carbon layer thickness of 300 nm. The SiC layer thickness was 100 nm for all the composites. Preparation conditions of the polymeric slurries were determined based on previous studies.[16),17)] The PMMA particles were mixed with the AHPCS liquid at an outer percentage of 64 wt % in the PSH-PIP process, while the SiC powder was mixed with the AHPCS liquid at an outer percentage of 30 wt % in the conv. PIP process. The slurry of the AHPCS liquid and PMMA particles was controlled for its fluidity by adding a hexane solvent at an outer percentage of 40 wt %. However, solvent was not added to the slurry of the AHPCS liquid and SiC powder. The mixing and polymer immersion were conducted in air. At the beginning of the vacuuming for the curing process, some amount of the slurry was squeezed out of the bag under atmospheric pressure. All pyrolyses were conducted up to 1000°C at a heating rate of 5°C/min with a holding time of 10 min. No external mechanical pressure was applied during any processing.

The composite plates were cut into various specimen shapes. Cross-sectional surfaces oriented perpendicular to the fiber-length direction were observed after the first and sixth densification process using a field emission scanning electron microscope (FE-SEM) S-4700 from Hitachi High Technologies Corp. (Japan). The surfaces of the composite were polished after the sixth densification process, while the surfaces of the composite were left as-cut after the first densification process because they were not sufficiently tough to be finely polished. Bulk densities and open porosities were measured for specimens of approximately $65 \times 8 \times 2\,mm^3$ using the Archimedean method using distilled water.

Basic mechanical properties of the composites were characterized using the tensile tests in the fiber transverse and longitudinal directions and also using the compressive test and the fracture toughness test in the fiber longitudinal direction. The transverse tensile test was performed for the rectangular specimens of size 30 (length) × 10 (width) × 2 (thickness) mm^3 with a gauge length of 20 mm at a crosshead speed of 0.2 mm/min. The longitudinal tensile test was carried out for the rectangular specimens of size $100 \times 80 \times 2\,mm^3$ with a gauge length of 50 mm at a rate of 0.5 mm/min. The compressive test was conducted according to the standard test from the Suppliers of Advanced Composite Materials Association (SACMA) SRM-1, in which a dumbbell specimen of 80 mm length and 2 mm thickness and a gauge area of size 15 (length) × 8 (width) mm^2 was compressively loaded at a rate of 0.2 mm/min. Fracture toughness was measured using the single-edge notched beam (SENB) method as specified in the Japanese Industrial Standards (JIS) R 1607. The rectangular specimens of size $40 \times 3 \times 4\,mm^3$ with a central straight notch of depth 1.5 mm were bent using a span length of 30 mm at a crosshead speed of 0.5 mm/min.

All the tests mentioned in the preceding section were performed using the electromechanical materials testing machine 5882 from Instron Corp. (US). A load cell with a maximum capacity of 100 kN was used with the testing machine for the longitudinal tensile test and the compressive test, and a load cell of maximum capacity 1 kN was used for the transverse tensile test and the SENB test. Five specimens were tested for each kind of composite in all the tests. Specimens used for the tensile tests were glued with cardboard sheets on those tab areas on both sides using Araldite® Standard from Huntsman International LLC (US). Ultimate stresses were calculated using the maximum loads in the test and the initial gauge areas, and were averaged to obtain a strength. Strain data from the longitudinal tensile test and the compressive test were obtained by averaging the data from strain gauges KFG-5-120-C1 supplied by Kyowa Electronic Instruments Co., Ltd. (Japan) attached on both sides of the specimens. Elastic modulus was calculated using the least squares method in each selected stress range as noted in Table 1.

Several experiments were conducted to examine the results of the mechanical tests. Fractography was carried out on post-test specimens using the FE-SEM as explained above and the micro X-ray CT, TOSCANER-30000μhd, from Toshiba Corp. (Japan). In-situ fiber strength was initially evaluated for the fractured specimens from the longitudinal tensile test in accordance with the procedure proposed by W. A. Curtin[18)] using a mirror constant of 2.51 $MPa \cdot m^{1/2}$.[19)] To compare the nominal rigidity and integrity of the matrix which reflected porosity and microstructural continuity, internal friction measurements were performed on the rectangular specimens of size $65 \times 8 \times 2\,mm^3$ using JE2-RT from Nihon Techno-Plus Co., Ltd. (Japan). In this measurement, a half-value width of the resonance peak of vibrational intensity as a function of frequency was used for the calculation.

3. Results and discussion

Scanning electron microscope (SEM) micrographs of the intra-bundle regions of the composites fabricated using the PSH-PIP process are shown in **Fig. 3**. Micrographs (a) and (b) show the microstructures after the first and sixth densification process,

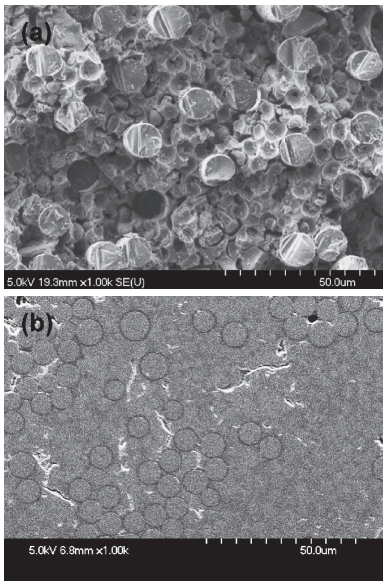

Fig. 3. SEM micrographs of the intra-bundle regions of the PSH-PIP composites after the (a) first and (b) sixth densification process.

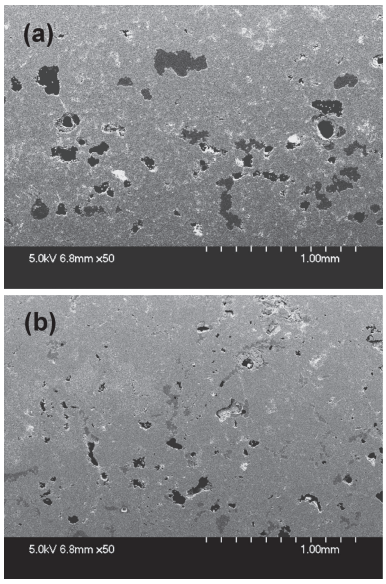

Fig. 4. SEM micrographs of wide areas showing the microstructure of the composites fabricated by (a) the conventional PIP and (b) the PHS-PIP process.

respectively. In micrograph (a), spherically-shaped pores, similar to those formed in monolices,[16] were observed among the fibers. This suggests that the pore-forming powder could well penetrate into the congested fiber interspaces in the unidirectional fiber sheets. The pores were partly filled with grained materials, namely polymer-pyrolyzed products, which would have been filled during the densification processes. This porous structure could be highly densified during the following five densification processes, as seen in micrograph (b). Round-shaped patterns which were identified in the matrix area were vestiges of the original porous structure. Thus, a polymer-derived porous base was well-produced even in the intra-bundle region by the first PSH-PIP process and was highly densified during the subsequent PIP processes. Meanwhile, for the conv. PIP process it has previously been verified that the intra-bundle region could be well-densified under the conditions employed in this study.[17]

The inter-bundle microstructure after the sixth densification processes was compared between the conv. PIP and the PSH-PIP composites. **Figures 4**(a) and 4(b) show the SEM micrographs of the composites fabricated using the conv. PIP and PSH-PIP processes, respectively. In micrograph (a), pores of diameter up to several 100 μm, which appear as black island regions, were distributed throughout the area. These regions are inter-bundle pores which extend somewhat along the fiber direction. On the other hand, those observed in micrograph (b) are markedly reduced in size.

This difference in pore distribution was assessed quantitatively using densitometry. Results from the densitometry measurements, amongst others, for the composites are summarized in Table 1. Two PSH-PIP composites show lower open porosities than the conv. PIP composite by more than 5%. This distinction is in good agreement with the above-mentioned analysis of their microstructures. There was no clear difference in the bulk density between the conv. PIP composites with a 300-nm-thick carbon layer and the PSH-PIP composites with a 300-nm-thick carbon layer. This result is attributed to the compositions of the composites: the SiC powder which is present only in the conv. PIP composite increased the apparent density due to its higher density ($\approx$3.2 g/cm^3) compared to that of the polymer-pyrolyzed product ($\approx$2.2 g/cm^3), leading the bulk densities of the conv. PIP composite to be heightened. Consequently, the bulk densities of the conv. PIP and the PSH-PIP composites with a 300-nm-thick carbon layer were nearly counterbalanced by the attributions of the SiC powder content and porosity. Here, it needs to be kept in mind that this is a relative comparison under the same consolidation condition and that the open porosities could be lowered by improving the consolidation technique. In that case, the uniformity of the fiber bundle alignment would be the key aspect.

The differences in the inter-bundle microstructure and the open porosity of the composites between the conv. PIP and the PSH-PIP composites were present using the same consolidation condition. These differences are therefore considered to be due to either the slurry condition or the polymer decomposition process during consolidation. The former possible cause, the slurry condition, cannot be the main factor because the slurries of both processes had fluidities high enough to bleed out from a bag at the beginning of the vacuuming and to migrate into the small intra-bundle region. Besides, any solvent was not added to the conv. PIP composites which contained more inter-bundle pores, because the solvent vapor generated by evaporation could form additional pores in the impregnated fiber sheet. With regard to the latter possible cause, the polymer decomposition process, the volumetric yield from polymeric slurry to pyrolyzed-product cannot be the major factor because the slurry used in the conv. PIP process ($\approx$41 vol.%) had a higher volumetric yield than that used in the PSH-PIP process ($\approx$13 vol.%). Instead, the major factor that causes the difference can be attributed to the morphological features during polymer decomposition. When a porous structure was initially formed in the matrix, space created by the polymer's volume shrinkage was considered to be dispersed more finely, so that inter-bundle pores became smaller and the polymer-pyrolyzed product distributed more uniformly in the fibrous preform, allowing the composite to be subsequently densified. In other words, the matrix base made by the PSH-PIP process would be more efficiently densified by the subsequent densification process owing to its higher specific surface.

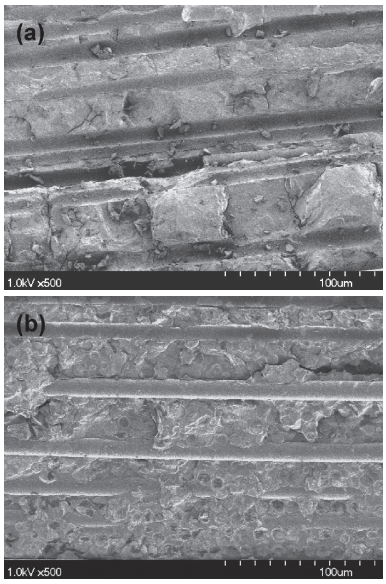

Fig. 5. SEM micrographs of the fracture surfaces of the composites fabricated by (a) the conventional PIP and (b) the PHS-PIP process after the transverse tensile test.

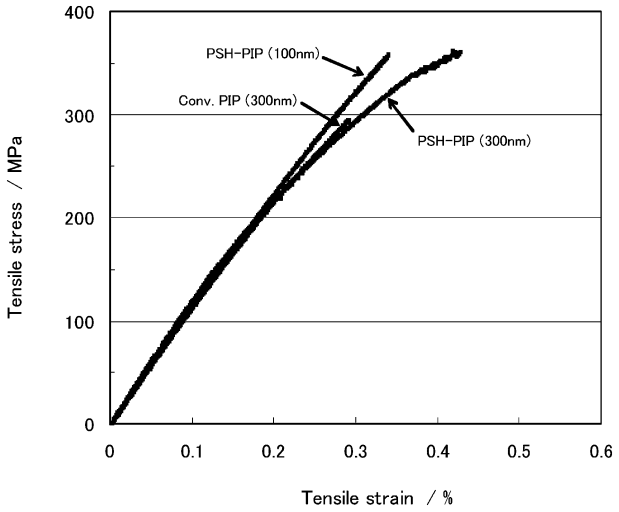

Fig. 6. Typical stress–strain curves of the composites obtained from the longitudinal tensile test.

Mechanical testing results are explained seriatim in the following. At first, let us describe the result of the transverse tensile test shown in Table 1. This compares the nominal stiffness of the matrix along the transverse direction between the conv. PIP composite and the two PSH-PIP composites. Though the standard deviations are large, the PSH-PIP composites exhibit more than twice the strength of the conv. PIP composite on average, and the two PSH-PIP composites had similar strengths independent of the interface carbon layer thickness. This would be mainly because the inter-bundle pore size was much reduced in the PSH-PIP composites compared to the conv. PIP composite. Therefore, these results demonstrate that a matrix fabricated by the PSH-PIP process is transversely much sturdier than that fabricated by the conv. PIP process.

Figures 5(a) and 5(b) show the SEM fractographs of the conv. PIP and the PSH-PIP composites after the transverse tensile test, respectively. In micrograph (a), a fracture surface that typically appeares in brittle materials is observed in the matrix region. Meanwhile, in micrograph (b), a particulate-shaped morphology is observed all over the matrix, which correspond to the vestigial characteristics of a porous structure fabricated by the first PSH-PIP process. Therefore, the fracture surface observed in this SEM micrograph reveals that fractures of the matrix might occur, largely reflecting the microstructures formed during the first process, even though the matrix was well-densified by the subsequent processes. This is perhaps due to the interfaces between the polymer-pyrolyzed products of the different PIP steps being relatively weak. This would also be related to the fact that the mechanical characteristics of a PIP-derived composite is affected by an initially-formed matrix to some extent.[11] This fact suggests that the PSH-PIP might reduce the nominal rigidity of the matrix due to an increased specific area of the interface in the matrix, though an accurate measurement of the elastic modulus wasn't carried out in this testing. The specific area of the interface is considered to be a possible influencing factor on the mechanical characteristics of the composites.

Longitudinal tensile strengths of the composites are shown in Table 1. All the composites exhibit strengths of over 300 MPa on average, which are quite preferable for composites of longitudinal fiber volume fraction of 20% as shown in Table 1. Furthermore, the PSH-PIP composites show a higher strength than that of the conv. PIP composite by about 12% and the two PSH-PIP composites have an almost equal strength despite the fact that the carbon layer thicknesses are different. Therefore, the difference in the longitudinal strength is attributed to the matrices produced by the first PIP processing rather than the interface layers. Possible causal factors for the fact that the matrix exerted an influence on the strengths would be porosity, size and shape distributions of the pores, or the micro-pore-based structure mentioned in the preceding paragraph.

Figure 6 shows typical stress–strain curves of the three composites obtained using the longitudinal tensile test. All the composites show similar near-linear behaviors in the initial stage up to around 200 MPa. Accordingly, the elastic moduli calculated in the range 0–100 MPa were fairly close to each other, as shown in Table 1. This indicates that the effect of the micro-pore-based structure on the rigidity of the composite, speculated above, is small. This is supported by the result from the internal friction measurement as shown in Table 1 in which the internal friction of the conv. PIP composite is higher than those of the PSH-PIP composites, probably depending on those porosities. The mechanical integrity may not be explicitly decreased by the PSH-PIP process-associated microstructure. From around 200 MPa, the curves of the conv. PIP composite and the PHS-PIP composite with a 300-nm-thick carbon layer started to deviate from the initial straight-line, with increasing strain. Owing to this pseudo-plastic behavior, the strain on the PSH-PIP composite with a 300-nm-thick carbon layer increased to as high as 0.4%. On the other hand, the PSH-PIP composite with a 100-nm-thick carbon layer maintains a linear behavior with increasing stress until approximately its ultimate stress at a strain of just more than 0.3%. This difference in the behaviors between these composites above 200 MPa was apparently due to the carbon layer thickness. In particular, the PSH-PIP composites with a 300-nm-thick carbon layer exhibit a larger elongation capability than the PSH-PIP composites with a 100-nm-thick carbon layer. So far, we found that the conv. PIP composite and the PSH-PIP composite with a 300-nm-thick carbon layer exhibited similar conditions of matrix nominal rigidity and interface elongation capability. There

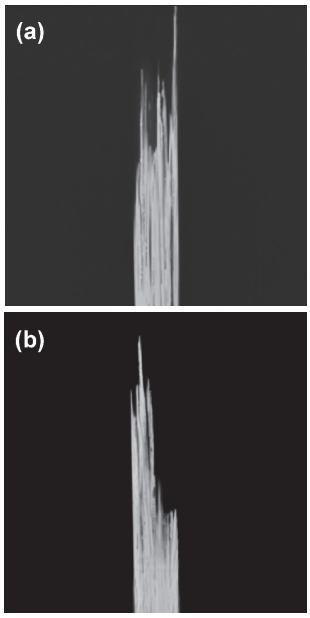

Fig. 7. Tomographic images of the fractured pieces of the composites fabricated by (a) the conventional PIP and (b) the PSH-PIP process after the longitudinal tensile test.

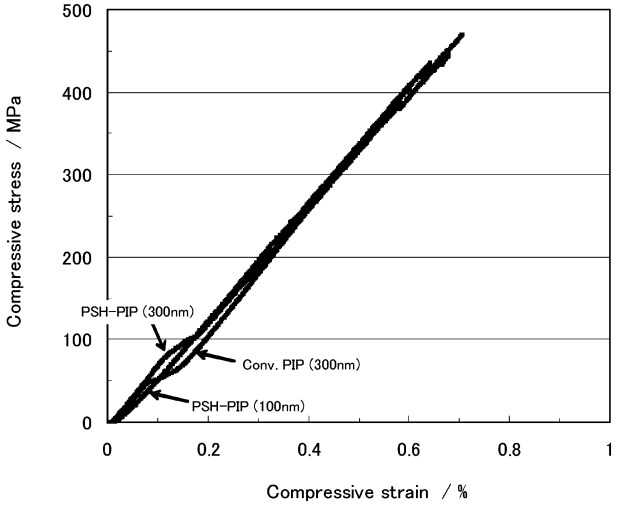

Fig. 8. Typical stress–strain curves of the composites obtained from the compressive test.

may be other factors that lead to a difference in those longitudinal tensile strengths between them.

The results of the longitudinal tensile test were further explored by examining the fracture appearance. Typical tomographic images of the entire fractured specimens from the longitudinal tensile test are shown in **Fig. 7**. The conv. PIP and the PSH-PIP composites with a 300-nm-thick carbon layer are shown in Figs. 7(a) and 7(b), respectively. The image of the PSH-PIP composite with a 100-nm-thick carbon layer was similar to that in Fig. 7(b). From these images, a holistic trend could be qualitatively identified, namely that the fibers of the conv. PIP composite broke more randomly into clusters along the longitudinal direction, leading to the formation of brush-like fracture areas comprised of broken fiber aggregations, whereas the fibers of the PSH-PIP composites broke at similar positions to each other and thus relatively simple fracture areas were formed. These trends can be rationalized by considering that the fiber bundles of the conv. PIP composite were not so firmly fixed to each other due to the large amount of inter-bundle pores, while the bundles of the PSH-PIP composites were substantially fixed by the denser matrix. Thus, the mechanical interactions between the bundles were relatively weak in the conv. PIP composite. This might also explain why the tensile strength of the conv. PIP composite is smaller than that of the PSH-PIP composites. One possible explanation is that when the mechanical continuity across the fibers is not ensured, in-situ fiber strengths and the proportion of fibers working effectively against the applied stress would be lower, leading to a reduction in the effective overall strength of the composites. This is supported in a preliminary evaluation of in-situ fiber strengths, where the tensile strength value of the conv. PIP composite (2.74 GPa) was found to be smaller than that of the PSH-PIP composite with a 300-nm-thick carbon layer (2.97 GPa). This issue needs to be studied in more detail.

Longitudinal compressive strengths of the composites are shown in Table 1. In this case, the two composites having the same carbon layer thickness of 300 nm showed almost the same strengths regardless of the difference in initial PIP process. Instead, the strengths differed depending on the interface layer thickness. The PSH-PIP composite with a 100-nm-thick carbon layer exhibit a lower strength than the other two composites by approximately 30%.

Figure 8 shows typical stress–strain curves of the composites obtained by the compressive test. On the whole, all the composites show nearly linear behaviors with similar slopes. Accordingly, compressive elasticity moduli calculated from their linear sections were relatively close to each other as shown in Table 1. The notable difference is that, in the curves of the two composites with a 300-nm-thick carbon layer, the slopes temporarily decreased at low-level stress below 100 MPa, whereas the slope of the composite with a 100-nm-thick carbon layer remained fairly constant throughout. The behaviors shown of the composites with 300-nm-thick carbon layers were attributed to the closing displacements of micro cracks and pores in the matrices which were accompanied by fiber-matrix sliding. Here, we found that a carbon layer thickness of 300 nm exhibits a higher sliding capability than that of 100 nm.

Tomographic images of the fractured specimens after the compressive test are shown in **Fig. 9**. The image of Figs. 9(a)–9(c) were taken from the conv. PIP, PSH-PIP (300 nm) and PSH-PIP (100 nm), respectively. In the image of Fig. 9(a), microfractures were caused in an oblique direction at the center of the specimen. This seems to be a kinking failure along the principle plane of stress. In the image of Fig. 9(b), microfractures spread around the gauge part of the specimen accompanied by some splits. In the image of Fig. 9(c), a certain number of splits predominantly occurred. The most notable difference between the three fracture images is that the failures shown in Figs. 9(a) and 9(b) are mainly comprised of micro-sized fractures whereas splits are predominant in Fig. 9(c). Small-sized fractures are considered to occur under conditions where load redistribution mechanics, via fiber-matrix interface sliding, are sufficient enough to avoid wide-range crack initiation. On the other hand, splits would predominantly occur when an interface sliding function was not so high as to enable sufficient load redistribution. The data from Fig. 8 already suggests that the composites composed of 300-nm-thick carbon layers have a higher load-redistribution capability than that of a 100-nm-thick carbon layer. Therefore, we can conclude that the compressive strength was mainly influenced by an interface property; it should be controlled so that it provides

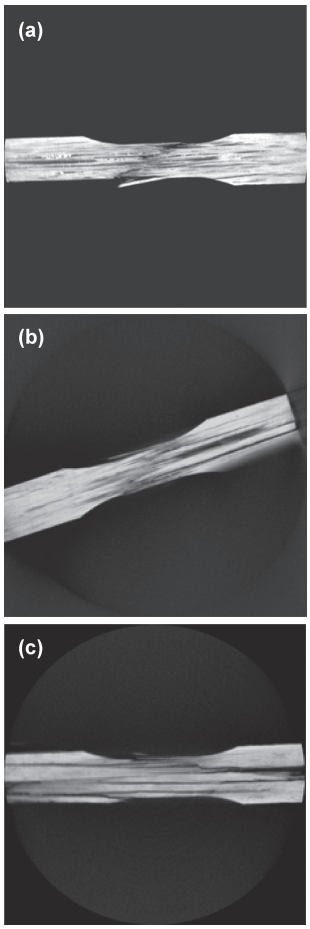

Fig. 9. Tomographic images after the compressive test of the fractured specimens of the composites fabricated by (a) the conventional PIP process, (b) the PSH-PIP (300 nm) process, and (c) the PSH-PIP (100 nm) process.

enough load redistribution capability to avoid splitting. Meanwhile, as for the difference between the images of Figs. 9(a) and 9(b), a kinking failure as in the former case might occur only because its structural stability in a lateral direction was relatively lower due to a larger amount of pores while such a failure was suppressed in the latter case because of its relatively higher structural stability.

Finally, the result of the SENB test shown in Table 1 is described. Because a portion of the specimens is fractured with interlaminar crack propagation, these values were regarded as reference information for fracture toughness. The value obtained for the conv. PIP composite was approximately two-thirds of those of the other two PSH-PIP composites. This is considered to be closely related to the degree of matrix densification. Thus, it was demonstrated that the improvement in matrix density accomplished by the PSH-PIP processing is advantageous to increase fracture resistance.

4. Conclusions

In order to improve the matrix microstructure of PIP-derived SiC/SiC composite, a combined process of PIP process with a porous-producing treatment (the PSH-PIP process) was examined. The following advantageous results were obtained:

i) The precursor slurry that was prepared based on the previously conducted study was well impregnated into a unidirectional fiber sheet, and a micropore-filled matrix base was produced even in the intra-bundle region.
ii) The porous matrix bases made from the first PSH-PIP process were more efficiently densified by the subsequent PIP processes, and consequently composites with lower porosity containing much smaller inter-bundle pores were produced.
iii) The composites with improved matrices made using the PSH-PIP process showed excellent properties in terms of transverse and longitudinal tensile strengths.

Acknowledgements This work was carried out as part of the R&D activity of the Space Open Lab program operated by the Japan Aerospace Exploration Agency (JAXA). The authors acknowledge the various experimental support provided by JAXA staff Ms. Hisako Gushima, Ms. Junko Aoki and Mr. Yorimichi Saito.

References

1) F. Christin, Proc. 4th Int. Conf. High Temp. Ceram. Matrix Comp. (2001) pp. 731–743.
2) R. Naslain, *Comp. Sci. Tec.*, **64**, 155–170 (2004).
3) T. Ishikawa, *Ceramics*, **36**, 27–31 (2001) [in Japanese].
4) J. A. DiCarlo, 6th Int. Conf. High Temp. Ceram. Matrix Comp. New Delhi, Sep. 4–7 (2007).
5) D. E. Glass, Proceedings of 15th AIAA International Space Planes and Hypersonic Systems and Technologies Conference, AIAA-2008-2682 (2008) 1–36.
6) K. Handrick, H. Lange, M. Leuchs, A. Steinacher and S. Weiland, Proc. 7th Int. Conf. High Temp. Ceram. Matrix Comp. (2010) pp. 499–504.
7) S. Yajima, T. Shishido and K. Okamura, *Ceram. Bull.*, **56**, 1060–1063 (1977).
8) B. E. Walker, R. W. Rice, P. F. Becher, B. A. Bender and W. S. Coblenz, *Ceram. Bull.*, **62**, 916–923 (1983).
9) B. A. Bishop, M. S. Spotz, W. E. Rhine, H. K. Bowen and J. R. Fox, in: G.L. Messing, E.R. Fuller, H. Hausner (Eds.), Ceramic powder science II vol. 1, Am. Ceram. Soc. Westerville (OH) (1987) pp. 856–863.
10) W. H. Atwell, G. T. Burns and G. A. Zank, in: J.F. Harrod, R.M. Laine (Eds.), Inorganic and Organometallic Oligomers and Polymers, Kluwer Academic Publisher, Netherlands (1991) pp. 147–159.
11) M. Kotani, T. Inoue, A. Kohyama, K. Okamura and Y. Katoh, *Comp. Sci. Tech.*, **62**, 2179–2188 (2002).
12) M. Kotani, T. Inoue, A. Kohyama, Y. Katoh and K. Okamura, *Mater. Sci. Eng., A*, **357**, 376–385 (2003).
13) W. A. Curtin, *J. Am. Ceram. Soc.*, **74**, 2837–2845 (1991).
14) K. Nishiyabu, S. Matsuzaki and S. Tanaka, *J. Jpn. Soc. Powder Powder Metallurgy*, **53**, 776–781 (2006) [in Japanese].
15) K. Nishiyabu, in: D.F. Heaney (Eds.), Handbook of Metal Injection Molding, Woodhead Publishing Ltd., Cambridge (2012) pp. 349–390.
16) M. Kotani, K. Nishiyabu, S. Matsuzaki and S. Tanaka, *J. Ceram. Soc. Japan*, **119**, 563–569 (2011).
17) M. Kotani, Y. Katoh, A. Kohyama and M. Narisawa, *J. Ceram. Soc. Japan*, **111**, 300–307 (2003).
18) W. A. Curtin, *J. Am. Ceram. Soc.*, **77**, 1075–1078 (1994).
19) A. J. Eckel and R. C. Bradt, *J. Am. Ceram. Soc.*, **72**, 455–458 (1989).